Informatics in Medicine Unlocked 13 (2018) 62–70

Contents lists available at ScienceDirect

Informatics in Medicine Unlocked

journal homepage: www.elsevier.com/locate/imu

Analysis of flow patterns on branched endografts for aortic arch aneurysms

T.L. Chiu[a,*], Abraham Y.S. Tang[a], Stephen W.K. Cheng[b], K.W. Chow[a]

[a] Department of Mechanical Engineering, University of Hong Kong, Pokfulam, Hong Kong
[b] Department of Surgery, Li Ka Shing Faculty of Medicine, University of Hong Kong, Pokfulam, Hong Kong

ARTICLE INFO

Keywords:
Aortic aneurysms
Endovascular treatment
Internally directed side branches
Computational fluid dynamics (CFD)
Helicity flow index (HFI)

ABSTRACT

Objective: Rupture of aneurysm on the aortic arch leads to significant rates of mortality. Traditional surgical repair is traumatic and may be inappropriate for some patients. Deployment of internally directed side branches provides a feasible alternative, but the hemodynamic implications have not been fully investigated and will be addressed in this study.
Method: Both patient specific pre- and post-operative conditions are treated here with computational fluid dynamics. Quantitative indicators like volume flow rate, wall shear stress and helicity index are employed.
Results: Changes in volume flow are generally mild unless an antegrade branch is utilized. Wall shear stress reveals a fluctuating and complex flow pattern between the brachiocephalic and left subclavian artery after graft implantation. Circumferentially averaged oscillatory shear indices at the left common carotid artery are in the range of (0.18, 0.26). Helical flows are observed both before and after surgical repairs, and are measured by spatially integrated helicity and a 'helicity flow index'. Before surgical implant of grafts, blood flows frequently display a predominant direction of rotation. This feature is typically diminished after the implantation.
Conclusion: In general, aortic blood flow displayed a higher degree of oscillatory and helical features after internal side branches were deployed. Clinically, oscillatory flows may promote blood clot formation. Furthermore, flow separation points near the outer wall of internal side branches induce fluctuations in pressure and force which might threaten the integrity of the stent graft. To achieve the goal of side branch patency, proper stent orientation is thus critical.

1. Introduction

Degenerative aneurysm of the aortic arch is a disease of the aged and is becoming more common as life expectancy increases with improved health care. On reaching a certain size, about 40% of arch aneurysm ultimately ruptures within two years of diagnosis [1], and others cause vocal cord palsy, leading to hoarseness and respiratory complications.

As such aneurysms are anatomically located near key vessels supplying blood to the brain and upper limb, surgical repair remains the greatest challenge of cardiovascular surgery. Traditional open repair requires a sternotomy, cardiopulmonary bypass, and deep hypothermic circulatory arrest. Such ultra-major procedures are only tolerated by a minority of patients, and risks of death (10%) and stroke (20%) remain high. There is no effective treatment for those deemed unfit for surgery. Hybrid procedures covering the arch with an off-the-shelf tube thoracic stent graft in combination with various "debranching" operations, or carotid chimneys, are temporary alternatives and were never widely accepted due to their extra-anatomical nature of directing blood flow.

Recent advances in endovascular treatment now encompass a minimally invasive option of treating arch aneurysms [2]. The aneurysm is excluded by custom made stent grafts landing proximally in the ascending aorta, and distally in the descending aorta, with cerebral revascularization achieved by one, two or three internally directed side branches [3]. Such aortic arch branched endografts sit at the epitome of vascular surgery. Currently only three medical centers in Japan and Hong Kong have experience in performing this type of advanced repair.

While early results are promising and certainly can benefit high risk patients, the complication rate remains high, most notably post-operative stroke [4,5]. Factors such as flow impairment, or embolization during the procedure, to post-operative branch occlusions and hypoperfusions may be critical. Another major concern is retrograde aortic dissections, caused by the mismatch of tissue compliance between the prosthetic and native portion of the high stress ascending aorta. These known risks may occur unpredictably and can be difficult to control even at the most experienced centers. Long term results are as yet unknown, and concerns of occlusions of the side branches and their catastrophic complications of ischemic stroke are valid.

* Corresponding author.
E-mail address: u3003609@connect.hku.hk (T.L. Chiu).

https://doi.org/10.1016/j.imu.2018.10.008
Received 21 August 2018; Received in revised form 8 October 2018; Accepted 16 October 2018
Available online 18 October 2018

Custom designs of the aortic arch branched stent grafts revolve around changes in the graft diameter, the carotid artery side branch location, side branch diameter, and take off angles based on their location in the arch. Antegrade and retrograde pointing side branches are possible. Other anatomically determined parameters include the anterior-posterior curvatures and the acuteness of the aortic arch.

Until recently, it was not possible to determine the effect of different designs of these endografts on the hemodynamics. Novel computational schemes can simulate flow in and outside the branches, and determine high stress areas (predisposing to retrograde dissection) [6]. Fluctuations in pressure and shear stress can impose detrimental effects on the stent graft [7]. This study aims to acquire quantitative hemodynamic data after the implant of internally directed side branches, as the blood flow pattern may be drastically altered. Knowledge of flow patterns and the relevance of the associated medical implications are likely still far from complete. This study helps to shed light on complex hemodynamics phenomena and to identify potentially adverse effects. CFD simulation has not been performed on this novel surgical technique. Helicity was proposed as an informative indicator, consistent with a previous study on the aortic arch [8], where it serves as a useful tool in quantifying blood flow pattern in the aortic arch.

Since each patient is anatomically unique, such computational methods, based on a pre-procedural CT scan and three-dimensional modelling, can provide surgeons with a tool in designing grafts, as well as predicting success, immediate complications, and long term patency of the branches.

2. Materials and methods

2.1. Patients and imaging data

CT images covering the aortic root, ascending aorta, aortic arch and proximal descending aorta of a male patient with arch aneurysm were acquired with injection of 130 ml of contrast agent (Fig. 1). Endovascular repair was performed previously.

2.2. Geometrical model

Simulations were performed to assist a planned three-branched endografting surgical repair. CT imaging data in DICOM format were processed by the software Mimics (Materialise, Leuven, Belgium). The generated STL file was treated by SolidWorks (Dassault Systèmes SolidWorks Corp.S.A., France). Geometrically, the centerline was traced from descending aorta to aortic valve through 3D images, and a reconstructed aorta of 34 mm followed the endograft provided by the manufacturer. Similarly, three internal side branches corresponding to the brachiocephalic artery (BCA), left common carotid artery (LCCA) and left subclavian artery (LSA) were constructed with diameters of 12, 8 and 12 mm respectively. This Post-Thoracic-Endovascular-Repair (TEVAR) patient-specific geometry serves as the baseline benchmark, with additional models to elucidate the hemodynamics:

(1) a T-EVAR with one internal side branch to each branching artery, with the BCA, LCCA branch antegrade pointing, but the LSA retrograde, centerline of all vessels following that of the patient; The other configurations are similar to (1) but with slight modifications:
(2) LSA not antegrade;
(3) branches to BCA and LCCA extending proximally by 1 cm;
(4) branches to BCA and LCCA retracting distally by 1 cm;
(5) aneurysm being absent and no internal side branch inserted.

The schematic diagrams of the five simulated conditions are shown in Fig. 2.

Meshes for computational fluid dynamics (CFD) software were generated with the fluid domain covered by an unstructured tetrahedral grid. Mesh sizes varied from 3 mm to 0.5 mm and consisted of 1.0×10^6 to 1.1×10^6 cells [9], with finer grid being adopted near the entrance of side branches for higher resolution. The mesh independence test for these aortic arch simulations was reported earlier in the literature [9] and similar mesh sizes were adopted here too. A boundary layer of brick cell with aspect ratio of two was deployed near the wall.

2.3. Fluid mechanics and boundary conditions

CFD simulations were performed via FLUENT 17.1 (ANSYS, Canonsburg, Pennsylvania, USA). The underlying principles are mass conservation and momentum balance, governed by the continuity and Navier-Stokes equations (Eq. (1) and Eq. (2) respectively):

$$\frac{\partial u_i}{\partial x_i} = 0 \tag{1}$$

$$\frac{\partial u_i}{\partial t} + u_j \frac{\partial u_i}{\partial x_j} = -\frac{1}{\rho}\frac{\partial p}{\partial x_i} + \frac{\mu}{\rho}\frac{\partial^2 u_i}{\partial x_j \partial x_j} \tag{2}$$

where u_i (i = 1,2,3) are the components of velocity, x_i (i = 1,2,3) are the Cartesian spatial coordinates, and t, ρ, p and μ are time, fluid density, pressure and dynamic viscosity respectively. Repeated indices imply summation. Blood was taken as an incompressible and Newtonian fluid with a constant density and viscosity of 1060 kg/m^3 and 0.0035 kg/m s, respectively [10,11].

A segregated method, SIMPLE, was used as the pressure-velocity coupling scheme and second order upwind was used in momentum discretization. The evolution was traced by a first order implicit scheme with step size 0.001s. Convergence is achieved if the residual error dropped to 10^{-6}. Earlier works in the literature on aortic arch simulations [12] had demonstrated time grid independence for sufficiently small step size, and similar criteria would be utilized in the present work. Rigid wall was assumed and no-slip boundary condition was applied [13]. A cardiac cycle (T) of 1s was used. Periodicity was typically achieved after three cycles, and data there were analyzed.

Physiologically realistic pulsatile velocity profile using the Womersley solution and flow rate with an average value of 73.6 ml/s were imposed at the ascending aorta (Fig. 1) [14,15]. Theoretically, a unidirectional velocity field, periodic in time and axisymmetric in cylindrical polar coordinates was sought, resulting in a Fourier series description mathematically:

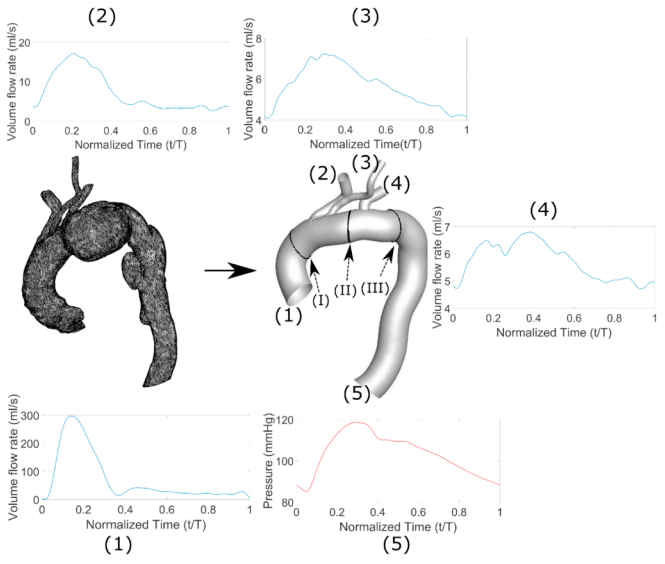

Fig. 1. Patient-specific geometry before and after the endovascular repair; (1) volume flow rate at ascending aorta, (2)–(4) volume flow rate at individual arch branches, (5) pressure wave form at descending aorta; (I), (II), (III) were the slicing plane for WSS parameters and streamlines extraction.

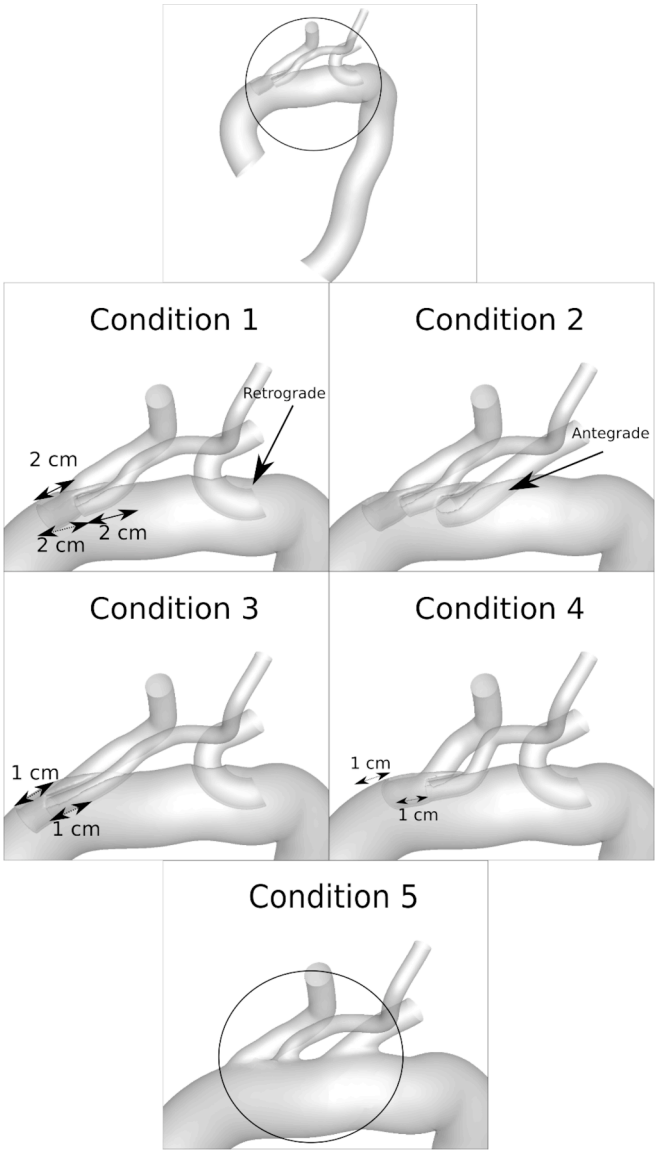

Fig. 2. Top: Area inside the circle was enlarged to illustrate the difference among the different conditions. Condition 1: Lengths of the internally directed side branches inside the main graft and their separation were marked, a retrograde LSA graft was highlighted. Condition 2: An antegrade LSA graft was used. Condition 3: BCA and LCCA grafts were extended proximally by 1 cm. Condition 4: BCA and LCCA grafts were retracted distally by 1 cm. Condition 5: Aneurysm was absent and no internal side branch was inserted.

$$u(r,t) = \frac{2a_0}{\pi R^2}\left[1-(\frac{r}{R})^2\right] + \Re\sum_n \left\{ \frac{a_n\cos(n\omega t) + b_n\sin(n\omega t)}{\pi R^2} \times \left[\frac{1 - \frac{J_0(\alpha_n \frac{r}{R} i^{\frac{3}{2}})}{J_0(\alpha_n i^{\frac{3}{2}})}}{1 - \frac{2J_1(\alpha_n i^{\frac{3}{2}})}{\alpha_n i^{\frac{3}{2}} J_0(\alpha_n i^{\frac{3}{2}})}} \right] \right\} \quad (3)$$

where a_n and b_n are the Fourier series coefficients of the inlet volumetric flow rate, ω is the angular frequency, R is the inlet radius, J_0 and J_1 are the Bessel functions of the first kind of the zeroth and first order respectively. $\Re$ indicates the real part of the expression. The parameter $\alpha = R\sqrt{\rho\omega/\mu}$, is the dimensionless Womersley number where ρ and μ are the density and dynamic viscosity respectively. It measures the ratio of unsteady inertia force due to pulsations to the viscous force. The parameter α_n employed in Eq. (3) is defined as $\sqrt{\rho n\omega/\mu}$. A user-defined function was implemented to incorporate this velocity profile with the flow solver. Besides the axial component of velocity at the aortic inlet, secondary flow was not properly accounted for, even though the existence of a swirling flow component of the cardiac output from the left ventricle had been concretely demonstrated by researchers [16–18]. However, echocardiographic information and patient-specific MRI data were generally difficult to obtain. Moreover, the magnitude or even the direction of rotation varied from patient to patient. Hence, only the most important velocity component was incorporated. At the descending aorta, pressure waveform with systolic/diastolic values of 122/82 mmHg was imposed (Fig. 1) [19]. Pressure waveforms for the branching arteries were determined by performing a simulation on Condition 1, which acted as the baseline, with a set of volumetric flow rates from the literature [14] specified to branching arteries. The set of area-averaged pressure waveforms was then obtained after this simulation. This set of pressure wave forms was then used in the subsequent simulations for other configurations of side branch deployments. The only exception was Condition 5 (no side branch insertion), where the reference volume flow rate was assigned. The choice of boundary conditions is always critical in computational fluid dynamics and two remarks here will be instructive. Firstly, by imposing a pre-determined pressure waveform at the outlets, the resistance of peripheral arteries may thus already be implicitly defined. Varying the downstream pressure patterns can provide a systematic study of peripheral resistance. Secondly, a more elaborate outlet condition involving the coupling of a lumped parameter, 1D model of the downstream domain, with the outflow boundaries of the 3D simulation domain was well noted [20,21]. Further studies along these directions will be taken up in the future.

The Reynolds number at peak systole, Re_{peak}, and the Womersley number α were 3374 and 24 respectively. The Dean number, which takes into account both the Reynolds number and the effect of curvature, was defined as

$$De = \sqrt{R/R_c}\,Re \quad (4)$$

where R is the inlet radius and R_c is the distance from the center of curvature to the centerline of the pipe. The value is about 1790 at peak systole. The resistance of a curved pipe becomes progressively higher as the curvature increases (or as R_c decreases) [22]. For pulsating flow, the Reynolds number for the transition to turbulence will require more additional input than the corresponding threshold in steady flow. Besides inertial and viscous forces, unsteady effects involving acceleration and deceleration, as well as flows in curved pipes and Dean vortices types factors must also be considered. No simple criteria are expected. Aortic flow might be transitional. It is computationally expensive and scientifically difficult to simulate a transitional flow. Hence, laminar flow was assumed in the current simulations. It is one of the limitations of this study.

2.4. Hemodynamics parameters

Data visualization and calculations of hemodynamics parameters were implemented by using Tecplot 360 (Tecplot, Bellevue, WA, USA) and MATLAB (MathWorks, Natick, MA, USA).

2.4.1. Volume flow rate

Volume flow rates (VFR) into upper arch branches are critical parameters clinically and patency of all branches is of primary concern. VFR is defined as:

$$\textit{Volume flow rate} = \int \vec{u}\cdot d\vec{A} \quad (5)$$

2.4.2. Wall shear stress (WSS)

WSS is related to the tangential force acting on the wall by the fluid flow. WSS parameters capture the flow pattern near the wall and elucidate the near wall hemodynamics by providing insight into the

geometric effects of graft configurations. Three indices were utilized:

1) Oscillatory Shear Index (OSI) [23] characterizes the varying shear, where is the shear stress and T is one time period of the oscillating flow.

$$OSI = 0.5\left(1 - \frac{|\int_0^T \vec{\tau}\, dt|}{\int_0^T |\vec{\tau}|\, dt}\right) \tag{6}$$

2) Time-averaged WSS (TAWSS) suggests possible sites for pathological conditions such as atherogenesis. Low TAWSS is prevalent at atherosclerosis-prone sites [24].

$$TAWSS = \frac{\int_0^T |\vec{\tau}|\, dt}{\int_0^T dt} \tag{7}$$

3) Relative residence time (RRT) [25] highlights the area with oscillating and low WSS,

$$RRT = \frac{1}{(1 - 2^{*}OSI)^{*}TAWSS} \tag{8}$$

where $\vec{\tau}$ is the wall shear stress.

Quantification of WSS parameters were performed at three locations on the aortic arch, I) proximal to the origin of BCA, II) between LCCA and LSA, III) distal to the origin of LSA (Fig. 1) by comparing circumferentially averaged values.

2.4.3. Helicity

Aortic hemodynamics was further elucidated by helicity. The helicity of a fluid flow in a volume D is defined as [26]:

$$H = \int_D (\vec{u} \cdot \nabla \times \vec{u})\, dV = \int_D H_k\, dV \tag{9}$$

where $\vec{u}$ is the velocity vector, $\nabla \times \vec{u}$ is the vorticity vector and H_k is helicity per unit volume, helicity density. A purely two dimensional flow will have zero helicity, as these two vectors are orthogonal to each other [26]. Physiologically, helical flows in arteries may play a positive role in graft patency. Two versions of bulk descriptors were computed by integrating H_k over the fluid domain:

$$H_{V_i} = \frac{1}{V_i}\int_{V_i} H_k\, dV \tag{10}$$

$$H_{V_i-abs} = \frac{1}{V_i}\int_{V_i} |H_k|\, dV \tag{11}$$

H_{V_i} is the volume averaged helicity while H_{V_i-abs} measures the magnitude of helicity in the fluid domain. V_i is the volume of the fluid domain under investigation. It was used to normalize the helicity-based bulk flow descriptors. These bulk flow descriptors were first proposed in works earlier in the literature [8,27]. In terms of kinematics, H_k changes sign across a separation or reattachment lines [26]. Helicity is zero at the rigid wall boundary due to the no-slip boundary condition. Hence, the sign of the helicity density at the boundary volume grid, instead of the value at the boundary itself, was shown as contour plot at a chosen time (Fig. 3). The separation point or reattachment point could be located and flow conditions could be examined qualitatively. Time at mid-systolic, $T_{mid\text{-}systolic}$ = 0.25s, was chosen which represented a deceleration phase. After examining flow pattern across the whole cardiac cycle, this time instant was chosen as the flow in this deceleration phase was more complex and contained more flow separations and recirculation zones than other phases. Another quantity used in the literature is the local normalized helicity (LNH) [9,10,13,28–30], which measured the alignment of velocity vector and vorticity vector along a particle trajectory and is defined as [13]:

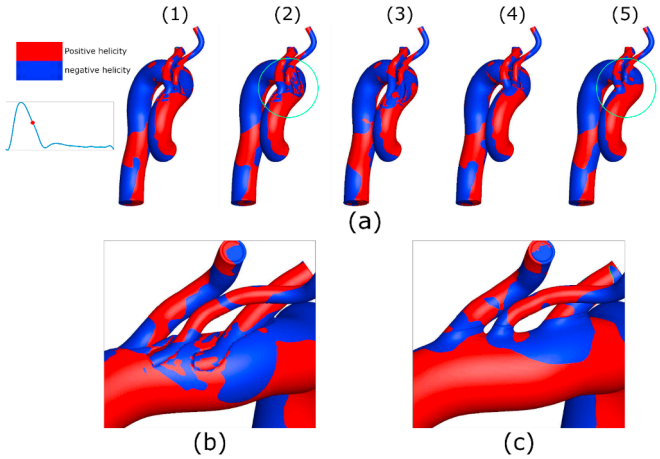

Fig. 3. Comparison of helicity sign at the center of boundary volume grid at $T_{mid\text{-}systolic}$; (a) Helicity contour plot for Conditions 1 to 5, from left to right; (b) & (c) Magnified region between brachiocephalic artery (BCA) and left subclavian artery (LSA) for Condition 2 & Condition 5, respectively.

$$LNH = \frac{\vec{u} \cdot \nabla \times \vec{u}}{|\vec{u}||\nabla \times \vec{u}|} \tag{12}$$

The magnitude ranges from unity for purely helical flow to zero for purely axial flow. A Lagrangian descriptor termed “Helicity Flow Index” (HFI) [13] was utilized to record the helical structure in the blood flow using information from LNH. Within a specific time interval, LNH experienced by the kth particle was recorded as hfi_k and HFI for that cluster of particles was calculated as:

$$hfi_k = \frac{1}{T_k^{end} - T_k^{start}} \int_{T_k^{start}}^{T_k^{end}} |LNH_k(\zeta)|\, d\zeta \tag{13}$$

$$HFI = \frac{1}{N_p}\sum_{k=1}^{N_p} hfi_k \tag{14}$$

hfi for each particle was calculated within a time interval $(T_k^{end} - T_k^{start})$, which was equal to one cardiac cycle or the time interval that the particle needed to leave the fluid domain when that interval smaller than one cardiac cycle. These definitions for hfi and HFI were first proposed in an earlier study [13]. In this study, N_p = 1000 massless particles were evenly distributed and released from the inlet at selected moments in time. HFI for that cluster of particles was calculated accordingly. At N_T = 5 different time instances, T_j, in systolic period, N_p particles were released. $\overline{HFI}$ value across these N_T cluster of particles for each condition was also computed. This method was first proposed in a previous study [31].

2.4.4. Streamline patterns

Instantaneous streamline patterns at various cross sections of the aorta were displayed alongside with the magnitude of the helicity. Quantifications of WSS parameters were performed for three typical cross sections too, where all such data were extracted at the time instant $T_{mid\text{-}systolic}$.

3. Results

3.1. Volume flow rate

Averaged values of VFR to all arch branches were summarized (Table 1). Condition 1 was used as the benchmark for normalization. Data of Condition 5 was included despite the difference in boundary conditions (VFR instead of pressure at the arch branches).

When the internal side branch for LSA was antegrade, the VFR

Table 1
Time-averaged volume flow rate to arch branches under different aortic geometries and percentage changes with respect to Condition 1.

	BCA		LCCA		LSA	
	Time-averaged VFR (ml/s)	Percentage changes (%)	Time-averaged VFR (ml/s)	Percentage changes	Time-averaged VFR (ml/s)	Percentage changes
1.)Baseline - aortic arch with internal side branches repair	7.29	–	5.63	–	5.71	–
2.)Antegrade LSA side branch, not retrograde	5.42	−25.66	5.17	−8.18	10.22	+79.06
3.)BCA & LCCA side branch extended proximally by 1 cm	7.49	+2.69	5.35	−4.97	5.87	+2.91
4.)BCA & LCCA side branch retracted distally by 1 cm	6.44	−11.67	5.59	−0.70	5.28	−7.45
5.)No internal side branch inserted	7.53	+0.87	5.88	+4.44	5.15	−9.71

would be larger than the original flow by 79%. By pulling the branches proximally, VFR would increase slightly for BCA and drop slightly for LCCA. In contrast, if they were both positioned 1 cm distally, BCA would receive 10% less blood and VFR to LCCA would remain unchanged. Moreover, VFR to LSA would also drop for the same geometric configuration.

3.2. Wall shear stress

Contour plots of WSS parameters reveal intriguing dynamics (Fig. 4). OSI has a more heterogeneous distribution when internal side branches are present in the model, especially for the region from the origin of BCA to that of LSA. A region of high OSI along the BCA and LCCA internal side branches implied a significant fluctuating flow pattern. This heterogeneous distribution was especially prominent in Conditions 2 and 3. RRT revealed a similar pattern to that of OSI. The region between the origin of BCA and origin of LSA also exhibited high RRT. Higher value of RRT was found along the BCA and LCCA internal side branches, especially in Condition 1, 3 and 4. In Condition 2, TAWSS was higher due to the higher VFR of LSA; hence, RRT along the outer wall of the internal side branches was not as high as other Conditions. In Condition 4, RRT has a large heterogeneous region around the BCA and LCCA internal side branches. When no internal side branch was present, no high RRT region was observed and the distribution was more homogeneous. TAWSS succinctly highlighted the region with large WSS. In Conditions 1 through 4, high WSS regions occur at the origin of all side branches. In particular, there was a region of high WSS near the origin of LSA for Condition 2.

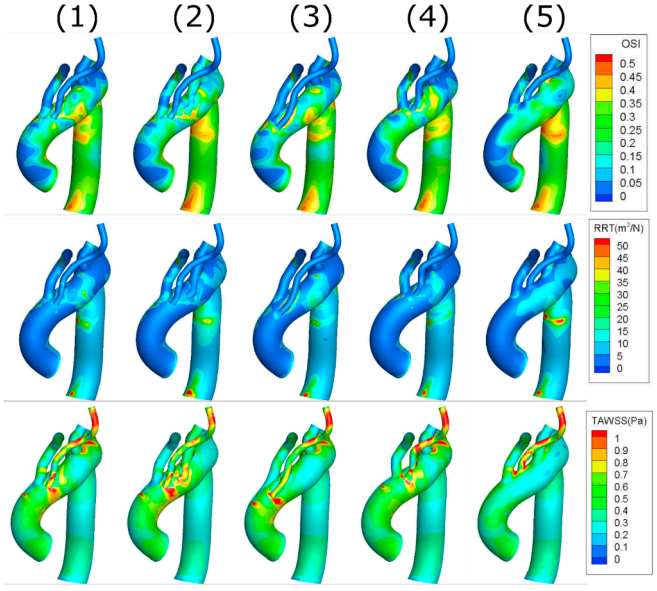

Fig. 4. Oscillatory Shear Index (OSI), Relative residence time (RRT) & Time-averaged WSS (TAWSS) contours in Conditions 1 to 5 respectively, each column represents one Condition.

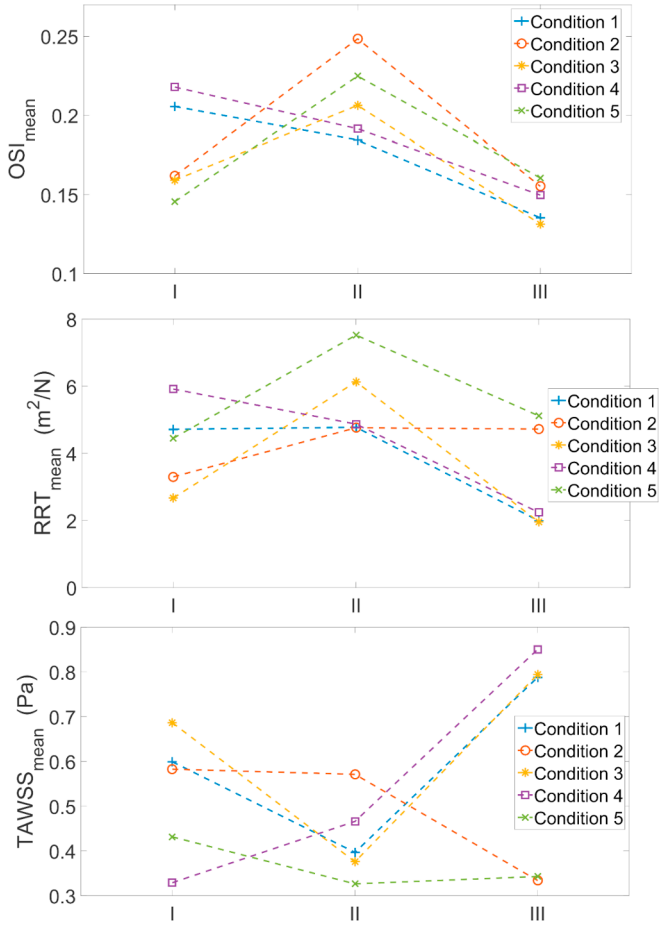

Fig. 5. Circumferentially averaged wall shear stress parameters at three different planes, (I) proximal to the origin of brachiocephalic artery (BCA), II) between left common carotid artery (LCCA) and left subclavian artery (LSA), III) distal to the origin of left subclavian artery (LSA).

Circumferentially averaged WSS results indicated that OSI has a higher value at Plane II in three Conditions (Fig. 5). Conditions 1 and 4 have a higher OSI at Plane I. For all Conditions, WSS was more oscillatory at Plane II than corresponding values at Plane III, the flow oscillates more between LCCA and LSA than region distal to LSA whether internal side branches are deployed or not. For RRT, Conditions 1 and 4 have a decreasing trend along the aortic arch. Condition 2 has a similar

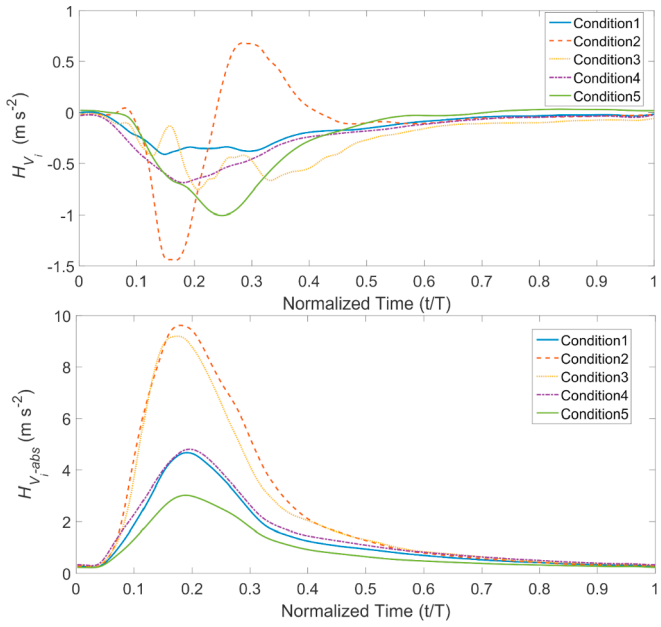

Fig. 6. The change of volume averaged helicity and helicity magnitude in the aortic arch throughout one cardiac cycle.

magnitude of RRT at Plane II and III due to the antegrade LSA side branches, which did not promote a higher WSS distal to LSA. Condition 3 has the highest RRT at Plane II, as the flow between the two branches was steadier than other Conditions, due to the increasing distance between the origins of LCCA and LSA. Conditions 1, 3 and 4 have similar values of RRT distal to LSA because of the retrograde LSA internal side branch. In general, aortic flow without the internal side branch has a higher RRT than those having such deployments. For TAWSS, Conditions 1, 3 and 4 have higher values distal to LSA. Condition 2 displayed a larger TAWSS at Plane II, while TAWSS was the lowest at Plane II for Condition 5.

3.3. Helicity

Helical flow patterns are prominent during the systolic phase, as highlighted by computational results of helicity (Fig. 6). For Condition 2, the dominant rotational nature of the flow changed sign frequently throughout the cardiac cycle, resulting in a numerically large value of H_{Vi-abs} compared with H_{Vi}. For Condition 5, a numerically significant negative H_{Vi} represented a strongly dominant counter-rotating flow (Fig. 6) and the actual absolute magnitude H_{Vi-abs} was the smallest among all of the Conditions. This implied a predominant direction of rotation in helical flow patterns. For Conditions 1, 3 and 4, the appearance of a dominant rotational direction was vastly diminished. All of these features on rotations effectively disappeared during the diastolic phase.

Bulk description in terms of time-averaged quantities are feasible too (Table 2). LCCA has the largest magnitude of helicity out of all Conditions due to the tortuous geometry. In BCA and LCCA, the helicity was reduced after internal side branches were inserted. In contrast, LSA has a higher helicity after graft deployment, regardless of antegrade or retrograde. When internal side branches were inserted in BCA and LCCA, the dominant rotational direction was not as prominent as that in Condition 5. While BCA has a larger $|H_{Vi}|$ in Conditions 1 and 2, LCCA exhibits larger $|H_{Vi}|$ in Conditions 3 and 4. Consequently, the proximal or distal nature of side branch deployment would have a significant effect on the preferred direction of rotation in BCA and LCCA. In terms of H_{Vi-abs}, BCA and LCCA had their smallest value in Condition 2, while LSA and aortic arch attain their maximum there. Antegrade internal side branch enhanced (reduced) the helicity in LSA and the aortic arch (in BCA and LCCA respectively).

The kinematics of helicity density is also illuminating (Fig. 3). The line between the two domains represented the separation or reattachment line [26]. Conditions with internal side branches generally had a more heterogeneous distribution of helicity, implying existence of more separation and recirculation zones. For Condition 2, where the LSA side branch was antegrade, the distribution near the origin of the three arteries was even more heterogeneous.

HFI values of particles released at five distinct instants in time summarized the quantitative aspect of the blood flow from a Lagrangian viewpoint. The release time, the resultant HFI and $\overline{HFI}$ are shown in Fig. 7(a), (b) and (c), respectively. In general, particles released at T_1 and T_5 experienced less LNH than particles released during the acceleration phase of peak systole. $\overline{HFI}$ for Condition 3 was lower than $\overline{HFI}$ of other Conditions.

3.4. Streamline patterns

Streamline patterns at $T_{mid\text{-}systolic}$ were investigated in terms of rotation and vorticity (Fig. 8). A pair of asymmetrically placed, counter-rotating helical vortices was observed for Conditions 1 through 3 at Plane I. However, only one vortex occurred for Conditions 4 and 5. At Plane II, one vortex was formed at the superior side of the stent graft for Conditions 1, 3 and 4, while a chaotic pattern arose for Condition 2, and a mild vortex was formed on the inferior side of stent graft in Condition 5. At Plane III, chaotic patterns with heterogeneous distribution of helicity resulted from the retrograde LSA side branch for Conditions 1, 3 and 4. For Condition 2 (5), two (one) well-structured vortices (vortex) were (was) formed respectively.

4. Discussion

Patient specific aortic arch branched stent graft was a novel technique to treat degenerative aneurysms, especially for those who were unfit for open surgery. By analyzing the helicity and WSS using realistic patient geometries, hemodynamics in a post-operative condition could be examined. Helicity quantifies the degree of rotation and spiral motion in the flow. This indicator is suggested to play a positive

Table 2
Time-averaged value of volume averaged helicity H_{V_i}, and helicity magnitude, H_{V_i-abs}, in various blood flow domains.

Volume domain	Averaged quantity	Condition 1	Condition 2	Condition 3	Condition 4	Condition 5
BCA	H_{Vi}	−0.152	−0.119	−0.077	0.077	−0.543
	H_{Vi-abs}	0.926	0.479	0.766	0.903	1.567
LCCA	H_{Vi}	0.210	0.078	−0.226	0.897	−2.001
	H_{Vi-abs}	3.120	2.639	2.875	3.582	3.715
LSA	H_{Vi}	0.210	0.675	0.085	0.086	−0.372
	H_{Vi-abs}	1.277	2.559	1.561	1.161	0.705
Aortic Arch	H_{Vi}	−0.149	−0.088	−0.257	−0.217	−0.217
	H_{Vi-abs}	1.336	2.451	2.294	1.485	0.937

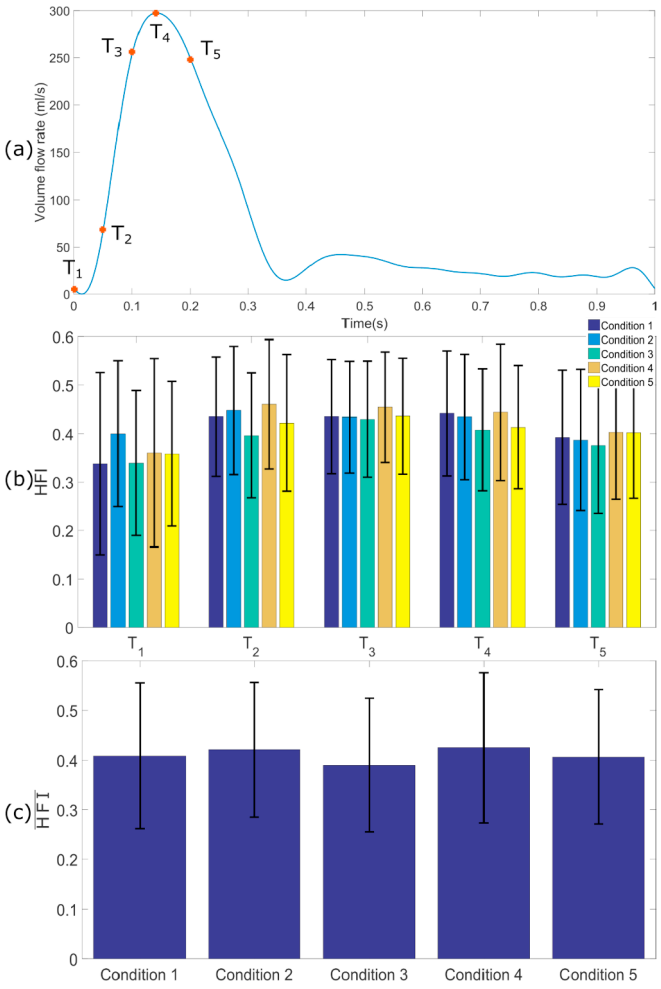

Fig. 7. (a) Five time moments during systolic period, T_j, when particles were released at the ascending aorta, (b) Helicity Flow Index (HFI) for different Conditions, standard deviation was calculated from the corresponding particle batch, (c) Averaged Helicity Flow Index (HFI) over all time moments for all 5 Conditions.

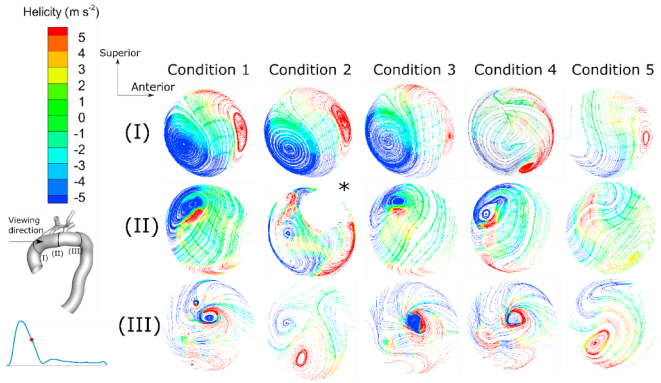

Fig. 8. Streamline plots for five Conditions at different slicing planes along the aorta. Each column corresponded to one Condition and each row corresponded to each slicing plane, (I), (II) and (III). Streamlines were taken at $T_{mid\text{-}systolic}$. (* represented the streamlines plot in which the excluded part was the entrance area of antegrade left subclavian artery graft).

physiological role in transporting blood efficiently, suppressing disturbed flow, and preventing accumulation of atherogenic particles on the arterial surfaces [27,32]. Here helicity was utilized to differentiate flow patterns in various internal side branch configurations quantitatively. WSS could reveal more information on the near wall hemodynamics.

Generally, a retrograde internal side branch impeded the flow to LSA (Table 1), as a higher pressure difference was needed to push the blood through the configuration. In Condition 2, an antegrade LSA branch increased the time-averaged VFR by nearly 80%. In this condition, BCA was affected most, and the average VFR decreased by 25%. LCCA was located between BCA and LSA and was less affected. By pulling the branches proximally, the path was less tortuous and the origins of the stent grafts were closer to the aortic valve. These result in a slight increase (decrease) in VFR to BCA (LCCA) respectively. Hence, the more proximal artery, BCA, has a larger suction effect when both BCA and LCCA side branches were put forward. In contrast, if they were both positioned 1 cm distally, the stent grafts would be slightly twisted, and the BCA would then receive less blood. At the same time, VFR to LSA would also be affected. The time-averaged VFR had an 8% decrease. This may arise from a slightly more chaotic flow by the retraction of the two stent grafts. The waveforms for the blood vessel from VFR to BCA were similar for all conditions, including the special case of condition 2 where the LSA branch was turned antegrade. Waveforms for the portion from the VFR to the descending aorta were similar among all conditions as well.

OSI was high in Condition 2, due to a significant volume influx of oscillatory flow to LSA. For Condition 3, the longer internal side branches generated more fluctuating vortices, and hence higher OSI along BCA and LCCA internal side branches. Elevated OSI indicated areas with fluctuating blood flow. Blood clots generally are formed by a cascade of coagulation proteins, especially under low shear stress condition or during time periods of rapid changes in shear stress [33,34]. Ischemic complications after EVAR may arise from clot embolization into the aortic side branches [35]. Regions of high TAWSS occurred at the origins of all side branches due to abrupt changes in cross-sectional areas for the blood flow. In particular, the region between LCCA and LSA was subject to oscillating flow because of the existence of internal side branches. Furthermore, the flow rate of LSA induced a higher TAWSS at the origin of the branch, regardless of the orientation of deployment (Figs. 4 and 5). High shear stress may trigger hemolysis as one of the possible complications after EVAR [36]. This shear induced hemolysis was highlighted in medical cardiovascular devices. Non-physiological shear stress may damage red blood cells and cause hemolysis. Hemolysis thresholds in different studies have suggested values in the range of 100–300 Pa [37]. However, with the onset of turbulence, the threshold can be reduced to 60 Pa. Although TAWSS at the origins were significantly below 60 Pa, instantaneous WSS could reach 20 Pa. Undesirable orientation of branches may thus cause hemolysis anemia, a feature of great relevance in the clinical care of patients.

The preferred rotational direction in LSA for Condition 2 was affected heavily by the high flow rate (Fig. 6), and blood flow pattern changed considerably. The final time-averaged results revealed that the helical content of the flow was enhanced by the high flow rate in LSA, but no dominant rotational direction arose. An extended internal side branch also generated more vortices along branches. Hence H_{Vi-abs} was high while $H_{Vi}$was lower due to the randomness and symmetry in creating those vortices. In other words, internal side branches created a more fluctuating and helical blood flow configuration, but this pattern did not retain a strong dominant rotational direction which would otherwise exist in a non-stented aortic arch [16,17]. Table 2 and Fig. 8 confirmed these statements, where predominant direction of rotation diminished in a post-operation condition, and a more chaotic flow pattern prevailed. From Table 2, this effect introduced a flow with a smaller degree of helicity to branching arteries. Comparison of H_{Vi-abs} between Condition 1 to 4 and Condition 5 for each artery verified this feature. As previously stated, helical flow serves as an atheroprotective role in the circulation system. Thus, the introduction of side branches reduced this protective effect, and caused the branching

arteries to be exposed to a more pathological condition. This novel surgical technique might thus generate a less physiological flow structure, which was different from some previous TEVAR [38] studied. In a healthy aorta, helical flow typically has a preferred direction, as demonstrated in an MRI acquisition study [17]. The helical flow helps to minimize turbulence in the upper arch [17]. The deployment of stent graft might diminish this effect, and actually aggravated the detrimental effects of turbulence (Fig. 6). Moreover, flow was more chaotic during the diastolic period, and prominent rotational direction was discerned.

4.1. Limitations

A remark on the limitations in the current research effort is in order. One simplification was the rigid wall assumption. The effect of wall motion can be critical. In addition to the curvature of the vessel and the pumping action of the heart, the motion of the aorta itself may also be a significant factor in blood flow patterns in the ascending aorta [39]. However, detailed analysis might pose a formidable challenge, since the mechanical properties of the stent graft and the thickness of the aortic walls were not accurately known.

Secondly, in the absence of patient-specific flow data to the aortic arch branches, typical volume outflows obtained from the literature [14] were utilized. The amount of blood entering arch branches varied among patients, and was influenced by many factors, e.g. resistance in the downstream vasculature, and body movement. Moreover, the inlet boundary condition included only the velocity component in the axial direction. Secondary flows or swirling components had been shown to exist in clinical imaging studies [17], and allowing for them should lead to additional insights [8]. Nevertheless, since comparisons were focused on pre- and post-EVAR flow conditions, assigning a set of typical VFR and ignoring secondary flow components were valid.

In terms of flow properties, a laminar regime was utilized instead of a turbulent one. However, patches of turbulent flows can occasionally be observed under normal and pathological conditions [40]. The Newtonian fluid assumption should be a valid one in aortic simulations, as the volume flow and shear rates were high. WSS or other near wall parameters must be calculated with caution, just like many other fluid dynamics situations involving boundary layers.

Another major limitation was the small sample size. Only one patient specific case was included. The aim of this study was to highlight the change in hemodynamics after EVAR. This patient specific case illustrated the potential risks. Ideally, more patient cases and in vivo clinical data should be used to validate these CFD results.

5. Conclusion

In this study, a quantitative assessment of the flow pattern and WSS on different endovascular repair conditions was performed. Simulations were implemented on different repair scenarios. Volume flow rate to arch branches, WSS pattern, helicity density, and Helicity Flow Index were used to analyze the effect and influence of the internal side branches. Results showed that the VFR was mildly affected by the stent graft, unless a retrograde graft was changed to antegrade. However, flow pattern and WSS distributions were altered dramatically. In general, blood flow was more oscillatory and more helical when internal side branches were present. This oscillatory flow promoted blood clot formation, and high shear stress may even cause hemolysis. Appropriate medication after surgery is needed to prevent blood clot embolization, and proper stent orientation is critical.

Clinically, EVAR may unfortunately trigger adverse consequences, such as promoting thrombosis in the limb. Limb occlusion can occur 4–5 years after EVAR. The mechanism of this thrombosis can be migration or dislocation of the stent graft. The fluctuation in WSS may affect the long-term integrity of the implanted side branches. The long term effects of the force acting on the stent graft could be a fruitful direction to further research [41]. Ultimately, this pilot study on internally directed side branches was meant to provide preliminary data and motivation for further research on this emerging technology.

Conflicts of interest

The authors declare that they have no conflict of interest.

Acknowledgments

Partial financial support was provided by the Innovation and Technology Support Program (ITS/150/15) of the Hong Kong Special Administrative Region Government.

References

[1] Yiu RS, Cheng SWK. Natural history and risk factors for rupture of thoracic aortic arch aneurysms. J Vasc Surg 2016;63(5):1189–94. https://doi.org/10.1016/j.jvs.2015.12.043.
[2] Cheng SWK. Novel endovascular procedures and new developments in aortic surgery. Br J Anaesth 2016;117. https://doi.org/10.1093/bja/aew222. ii3-ii12.
[3] Spear R, Clough RE, Fabre D, Roeder B, Hertault A, Martin Gonzalez T, Azzaoui R, Sobocinski J, Haulon S. Total endovascular treatment of aortic arch disease using an arch endograft with 3 inner branches. J Endovasc Ther 2017;24(4):534–8. https://doi.org/10.1177/1526602817714569.
[4] Spear R, Sobocinski J, Settembre N, Tyrrell MR, Malikov S, Maurel B, Haulon S. Early experience of endovascular repair of post-dissection aneurysms involving the thoraco-abdominal aorta and the arch. Eur J Vasc Endovasc Surg 2016;51(4):488–97. https://doi.org/10.1016/j.ejvs.2015.10.012.
[5] Spear R, Haulon S, Ohki T, Tsilimparis N, Kanaoka Y, Milne CPE, Debus S, Takizawa R, Kölbel T. Subsequent results for arch aneurysm repair with inner branched endografts. Eur J Vasc Endovasc Surg 2016;51(3):380–5. https://doi.org/10.1016/j.ejvs.2015.12.002.
[6] Rinaudo A, Raffa GM, Scardulla F, Pilato M, Scardulla C, Pasta S. Biomechanical implications of excessive endograft protrusion into the aortic arch after thoracic endovascular repair. Comput Biol Med 2015;66:235–41. https://doi.org/10.1016/j.compbiomed.2015.09.011.
[7] Fung GS, Lam SK, Cheng SW, Chow KW. On stent-graft models in thoracic aortic endovascular repair: a computational investigation of the hemodynamic factors. Comput Biol Med 2008;38(4):484–9. https://doi.org/10.1016/j.compbiomed.2008.01.012.
[8] Morbiducci U, Ponzini R, Gallo D, Bignardi C, Rizzo G. Inflow boundary conditions for image-based computational hemodynamics: impact of idealized versus measured velocity profiles in the human aorta. J Biomech 2013;46(1):102–9. https://doi.org/10.1016/j.jbiomech.2012.10.012.
[9] Singh SD, Xu XY, Wood NB, Pepper JR, Izgi C, Treasure T, Mohiaddin RH. Aortic flow patterns before and after personalised external aortic root support implantation in Marfan patients. J Biomech 2016;49(1):100–11. https://doi.org/10.1016/j.jbiomech.2015.11.040.
[10] Morbiducci U, Gallo D, Massai D, Ponzini R, Deriu MA, Antiga L, Redaelli A, Montevecchi FM. On the importance of blood rheology for bulk flow in hemodynamic models of the carotid bifurcation. J Biomech 2011;44(13):2427–38. https://doi.org/10.1016/j.jbiomech.2011.06.028.
[11] Morris L, Delassus P, Callanan A, Walsh M, Wallis F, Grace P, McGloughlin T. 3-D numerical simulation of blood flow through models of the human aorta. J Biomech Eng 2005;127(5):767–75. https://doi.org/10.1115/1.1992521.
[12] Tan FPP, Borghi A, Mohiaddin RH, Wood NB, Thom S, Xu XY. Analysis of flow patterns in a patient-specific thoracic aortic aneurysm model. Comput Struct 2009;87(11–12):680–90. https://doi.org/10.1016/j.compstruc.2008.09.007.
[13] Morbiducci U, Gallo D, Ponzini R, Massai D, Antiga L, Montevecchi FM, Redaelli A. Quantitative analysis of bulk flow in image-based hemodynamic models of the carotid bifurcation: the influence of outflow conditions as test case. Ann Biomed Eng 2010;38(12):3688–705. https://doi.org/10.1007/s10439-010-0102-7.
[14] Nauta FJ, Lau KD, Arthurs CJ, Eagle KA, Williams DM, Trimarchi S, Patel HJ, Figueroa CA. Computational fluid dynamics and aortic thrombus formation following thoracic endovascular aortic repair. Ann Thorac Surg 2017;103(6):1914–21. https://doi.org/10.1016/j.athoracsur.2016.09.067.
[15] Womersley JR. Method for the calculation of velocity, rate of flow and viscous drag in arteries when the pressure gradient is known. J Physiol 1955;127(3):553–63.
[16] Frazin LJ, Lanza G, Vonesh M, Khasho F, Spitzzeri C, McGee S, Mehlman D, Chandran KB, Talano J, McPherson D. Functional chiral asymmetry in descending thoracic aorta. Circulation 1990;82(6):1985–94. https://doi.org/10.1161/01.CIR.82.6.1985.
[17] Kilner PJ, Yang GZ, Mohiaddin RH, Firmin DN, Longmore DB. Helical and retrograde secondary flow patterns in the aortic arch studied by three-directional magnetic resonance velocity mapping. Circulation 1993;88(5):2235–47.
[18] Xenos M, Karakitsos D, Labropoulos N, Tassiopoulos A, Bilfinger TV, Bluestein D. Comparative study of flow in right-sided and left-sided aortas: numerical simulations in patient-based models. Comput Methods Biomech Biomed Eng 2015;18(4):414–25. https://doi.org/10.1080/10255842.2013.805210.
[19] Olufsen MS, Peskin CS, Kim WY, Pedersen EM, Nadim A, Larsen J. Numerical

simulation and experimental validation of blood flow in arteries with structured-tree outflow conditions. Ann Biomed Eng 2000;28(11):1281–99. https://doi.org/10.1114/1.1326031.
[20] Vignon-Clementel IE, Figueroa CA, Jansen KE, Taylor CA. Outflow boundary conditions for three-dimensional finite element modeling of blood flow and pressure in arteries. Comput Methods Appl Mech Eng 2006;195(29–32):3776–96. https://doi.org/10.1016/j.cma.2005.04.014.
[21] Les AS, Shadden SC, Figueroa CA, Park JM, Tedesco MM, Herfkens RJ, Dalman RL, Taylor CA. Quantification of hemodynamics in abdominal aortic aneurysms during rest and exercise using magnetic resonance imaging and computational fluid dynamics. Ann Biomed Eng 2010;38(4):1288–313. https://doi.org/10.1007/s10439-010-9949-x.
[22] Vester AK, Örlü R, Alfredsson PH. Turbulent flows in curved pipes: recent advances in experiments and simulations. Appl Mech Rev 2016;68(5):050802https://doi.org/10.1115/1.4034135.
[23] Ku DN, Giddens DP, Zarins CK, Glagov S. Pulsatile flow and atherosclerosis in the human carotid bifurcation. Positive correlation between plaque location and low oscillating shear stress. Arterioscler Thromb Vasc Biol 1985;5(3):293–302. https://doi.org/10.1161/01.ATV.5.3.293.
[24] Malek AM, Alper SL, Izumo S. Hemodynamic shear stress and its role in atherosclerosis. Jama 1999;282(21):2035–42. https://doi.org/10.1001/jama.282.21.2035.
[25] Himburg HA, Grzybowski DM, Hazel AL, LaMack JA, Li XM, Friedman MH. Spatial comparison between wall shear stress measures and porcine arterial endothelial permeability. Am J Physiol Heart Circ Physiol 2004;286(5):H1916–22. https://doi.org/10.1152/ajpheart.00897.2003.
[26] Moffatt HK, Tsinober A. Helicity in laminar and turbulent flow. Annu Rev Fluid Mech 1992;24(1):281–312. https://doi.org/10.1146/annurev.fl.24.010192.001433.
[27] Gallo D, Steinman DA, Bijari PB, Morbiducci U. Helical flow in carotid bifurcation as surrogate marker of exposure to disturbed shear. J Biomech 2012;45(14):2398–404. https://doi.org/10.1016/j.jbiomech.2012.07.007.
[28] Cheng Z, Kidher E, Jarral OA, O'Regan DP, Wood NB, Athanasiou T, Xu XY. Assessment of hemodynamic conditions in the aorta following root replacement with composite valve-conduit graft. Ann Biomed Eng 2016;44(5):1392–404. https://doi.org/10.1007/s10439-015-1453-x.
[29] Grigioni M, Daniele C, Morbiducci U, Del Gaudio C, D'Avenio G, Balducci A, Barbaro V. A mathematical description of blood spiral flow in vessels: application to a numerical study of flow in arterial bending. J Biomech 2005;38(7):1375–86. https://doi.org/10.1016/j.jbiomech.2004.06.028.
[30] Morbiducci U, Ponzini R, Rizzo G, Cadioli M, Esposito A, De Cobelli F, Del Maschio A, Montevecchi FM, Redaelli A. In vivo quantification of helical blood flow in human aorta by time-resolved three-dimensional cine phase contrast magnetic resonance imaging. Ann Biomed Eng 2009;37(3):516–31. https://doi.org/10.1007/s10439-008-9609-6.
[31] Morbiducci U, Ponzini R, Rizzo G, Cadioli M, Esposito A, Montevecchi FM, Redaelli A. Mechanistic insight into the physiological relevance of helical blood flow in the human aorta: an in vivo study. Biomechanics Model Mechanobiol 2011;10(3):339–55. https://doi.org/10.1007/s10237-010-0238-2.
[32] Morbiducci U, Ponzini R, Grigioni M, Redaelli A. Helical flow as fluid dynamic signature for atherogenesis risk in aortocoronary bypass. A numeric study. J Biomech 2007;40(3):519–34. https://doi.org/10.1016/j.jbiomech.2006.02.017.
[33] Gay M, Zhang LT. Numerical studies of blood flow in healthy, stenosed, and stented carotid arteries. Int J Numer Methods Fluid 2009;61(4):453–72. https://doi.org/10.1002/fld.1966.
[34] Fogelson AL, Neeves KB. Fluid mechanics of blood clot formation. Annu Rev Fluid Mech 2015;47:377–403. https://doi.org/10.1146/annurev-fluid-010814-014513.
[35] Maleux G, Koolen M, Heye S. Complications after endovascular aneurysm repair. Semin Intervent Radiol 2009;26(1):3–9. https://doi.org/10.1055/s-0029-1208377.
[36] Roselli EE, Idrees J, Greenberg RK, Johnston DR, Lytle BW. Endovascular stent grafting for ascending aorta repair in high-risk patients. J Thorac Cardiovasc Surg 2015;149(1):144–54. https://doi.org/10.1016/j.jtcvs.2014.07.109.
[37] Yen JH, Chen SF, Chern MK, Lu PC. The effect of turbulent viscous shear stress on red blood cell hemolysis. J Artif Organs 2014;17(2):178–85. https://doi.org/10.1007/s10047-014-0755-3.
[38] Gallo D, Lefieux A, Morganti S, Veneziani A, Reali A, Auricchio F, Conti M, Morbiducci U. A patient-specific follow up study of the impact of thoracic endovascular repair (TEVAR) on aortic anatomy and on post-operative hemodynamics. Comput Fluids 2016;141:54–61. https://doi.org/10.1016/j.compfluid.2016.04.025.
[39] Jin S, Oshinski J, Giddens DP. Effects of wall motion and compliance on flow patterns in the ascending aorta. J Biomech Eng 2003;125(3):347–54. https://doi.org/10.1115/1.1574332.
[40] Stalder AF, Frydrychowicz A, Russe MF, Korvink JG, Hennig J, Li K, Markl M. Assessment of flow instabilities in the healthy aorta using flow-sensitive MRI. J Magn Reson Imag 2011;33(4):839–46. https://doi.org/10.1002/jmri.22512.
[41] Tasso P, Raptis A, Matsagkas M, Rizzini ML, Gallo D, Xenos M, Morbiducci U. Abdominal aortic aneurysm endovascular repair: profiling post-implantation morphometry and hemodynamics with image-based computational fluid dynamics. J Biomech Eng 2018. https://doi.org/10.1115/1.4040337.

Mr. Tin Lok CHIU He is a part-time student at The University of Hong Kong. He holds the position of Medical Physicist at the Hong Kong Sanatorium & Hospital. The job duty is related to radiation oncology. He does NOT receive funding from any corporation which would inappropriately influence this work.

Dr. Abraham Yik Sau TANG He is a post-doctoral fellow at the University of Hong Kong during this research was performed. He has since then left the University for a consulting job in an engineering firm specializing in building services. He does NOT receive funding from any orporation which would inappropriately influence this work.

Prof. Stephen Wing Keung CHENG He is a Professor of Surgery at The University of Hong Kong, treating and caring for patients with vascular diseases. He does NOT receive funding from any corporation which would inappropriately influence this work.

Prof. Kwok Wing CHOW He is a Professor in Department of Mechanical Engineering at The University of Hong Kong, specializing in research in fluid mechanics and wave propagation. He does NOT receive funding from any corporation which would inappropriately influence this work.